Carbon Trends 5 (2021) 100135

Contents lists available at ScienceDirect

Carbon Trends

journal homepage: www.elsevier.com/locate/cartre

Amyloid-intercalated graphene oxide membranes for enhanced nanofiltration

Alice C. Lin, Fangyou Xie, Russell Chang, Nicholas Beaver, Claire Drewery, Catherine Collins, Corinne Lehr, Eric M. Jones, Shanju Zhang*

Department of Chemistry and Biochemistry, California Polytechnic State University, San Luis Obispo, CA 93407, USA

ARTICLE INFO

Article history:
Received 11 September 2021
Revised 3 November 2021
Accepted 14 November 2021

Keywords:
Hybrid membranes
Intercalation
Protein amyloid fibrils
Graphene oxide
Membrane nanofiltration

ABSTRACT

We report on fast pressure-driven nanofiltration of strong GO membranes intercalated by protein amyloid fibrils. We investigate the effect of protein amyloid fibril loading on membrane properties including the membrane stability, microstructure, reflux rate, permeance, rejection rate and fouling resistance. With increasing amyloid fibrils, the membrane becomes smooth and resilient and can be reused for many times with little disintegration. Microstructure analysis shows that amyloid fibrils enable expansion of the interlayer spacing between GO sheets, leading to around 100% increase in average water permeance of the 100 nm thick membrane (15.6 $L \cdot m^{-2} \cdot hr^{-1} \cdot bar^{-1}$) compared to the neat GO membrane (8.8 $L \cdot m^{-2} \cdot hr^{-1} \cdot bar^{-1}$). The hybrid membranes display improved moderate ion rejection (44–51%) of heavy metal salts and high molecular rejection (>97%) of organic dyes. Antifouling performance is evaluated in terms of flux recovery ratio and fouling ratios. The incorporation of amyloid fibrils enable GO membranes to change from irreversible fouling to reversible fouling and the hybrid membrane exhibits significantly enhanced flux recovery (>95%). A possible nanofiltration mechanism is proposed to explain the observations.

1. Introduction

Graphene oxide (GO) based nanofiltration membranes have demonstrated great potential for separation of molecules and ions in water treatment because of their well-defined nanochannels, surface functionalities and ease of synthesis and scale-up [1–3]. GO nanosheets are decorated with oxygen-containing functional groups including hydroxyl, epoxy, carboxyl and carbonyl groups on the basal planes and sheet edges. Typically, GO based nanofiltration membranes are composed of densely-packed GO nanosheets with an amphiphilic character, and the interlayer spacing between GO nanosheets acts as a 2D nanochannel for water permeation. Molecular separation in GO membranes is based on a combination of many factors including molecular sieving, adsorption and electrostatic interactions throughout nanochannels and functional groups [4–6]. Theoretical calculations [6–9] and experimental studies [10–12] have demonstrated that few-layer GO membranes have highly selective and permeable separations. However, GO membranes are in general unstable in aqueous media and easily disintegrate [13]. In addition, the water permeation of thick GO membranes is very low due to the small interlayer spacing and high tortuosity between GO sheets [14].

To date, one of the most effective ways to improve the stability and permeation of GO membranes is intercalating functional nanomaterials into GO nanosheets via physical mixing [15–19]. The incorporation of foreign nanomaterials not only expands the interlayer spacing between GO nanosheets for improved water permeation, but also generates strong interfacial interactions between the foreign particles and GO sheets for improved stability of the membranes. Various foreign nanomaterials, in particular 1D nanomaterials such as carbon nanotubes (CNTs) [20], polymer nanofibers [21], nanocellulose [22], and inorganic nanowires [15] have been studied in the fabrication of GO based hybrid membranes containing intercalated 1D and 2D nanostructures. Gao et al. reported CNT intercalated GO membranes with high water flux [20]. Acid treated CNTs served as a nanowedge to expand the interlayer spacing between GO sheets. As a result, the ion rejection of hybrid membranes decreased while the dye rejection rate remained as high as the neat GO membrane. Recently, Hung et al. reported hybrid membranes composed of silk nanofibers and GO [21]. Silk

* Corresponding author.
E-mail address: szhang05@calpoly.edu (S. Zhang).

https://doi.org/10.1016/j.cartre.2021.100135

nanofibers were assembled on the GO surfaces to increase the nanochannel size for accelerating water permeation. Hybrid membranes with the optimized ratio of silk nanofibers and GO displayed excellent stability, fast flux and more than 95% rejection of salts and dyes.

Amyloids are 1D fibrillar assemblies of proteins that are misfolded, often during the unfolding-refolding transition [23–25]. At the molecular scale, amyloids are characterized by a cross-beta quaternary structure in which parallel chains of beta-strands are oriented normal to the fibril axis. Amyloids have diameters of 5–15 nm and lengths of several micrometers, and they are emerging building blocks for artificial functional biomaterials [25–27]. In particular, amyloids possess excellent mechanical properties comparable with spider silk [28–31], and they may display a wide range of amino acids, which can serve as specific ion-binding sites [32–34]. These unique properties allow 1D amyloids to couple interactions with the oxygenated functional groups on 2D GO sheets, resulting in robust hybrid materials with mixed 1D and 2D nanostructures [32,35,36]. Recently, amyloid fibrils have been studied for effective removal of heavy metal ions and radioactive waste in water [37]. Typically, amyloid fibrils were incorporated into activated carbon yielding mechanically strong hybrid membranes. With optimization of the amyloid loading, the hybrid membranes efficiently absorbed pollutants and the removal efficiency was >99%. The membrane was sufficiently strong to reuse in filtering ten consecutive cycles without significant degradation of filtration. However, to the best of our knowledge, there has been no report on amyloid intercalated GO membranes for applications in water treatment.

In this work, we report on amyloid-intercalated GO membranes with varying GO/amyloid ratio for water purification. We find that the incorporation of amyloid fibrils reduces the surface roughness, increases the interlayer spacing and enhances the stability of GO membranes. Water permeance of hybrid membranes is double that of the neat GO membrane. The rejection of heavy metal ions (Cu^{2+} and Co^{2+}) increases with amyloid fibril content while the rejection of organic dyes remains above 97%. Bovine serum albumin is employed to evaluate fouling resistance of the membrane and >95% flux recovery of the hybrid membrane is discovered.

2. Experimental section

2.1. Materials

Graphite flakes, concentrated sulfuric acid (H_2SO_4), concentrated nitric acid (HNO_3), potassium persulfate ($K_2S_2O_8$), phosphorous pentoxide (P_2O_5), potassium permanganate ($KMnO_4$), hydrochloric acid (HCl), and hydrogen peroxide (H_2O_2), and β-lactoglobulin (βLG) from bovine milk were purchased from Sigma-Aldrich and used as received.

2.2. Preparation of graphene oxide

Graphene oxide was synthesized via the modified Hummers' method [38,39]. Typically, 5.0 g of graphite flakes was mixed with 200 mL of a mixture of 98% H_2SO_4 and 70% HNO_3 at a 3:1 vol ratio under stirring at room temperature for 24 hrs. The acid-treated graphite flakes were then rinsed with deionized (DI) water until the rinse pH = 4. The dried solid was heat treated in a furnace at 1000 °C for 10 s to obtain expanded graphene (EG). Next, 5.0 g of EG flakes and 300 mL of 98% H_2SO_4 were mixed in an ice bath, followed by the addition of 4.2 g of $K_2S_2O_8$ and 6.2 g of P_2O_5. The system was then transferred into an oil bath and the mixture was heated to 80 °C under stirring for 5 h. The pre-oxidized EG flakes were rinsed with water until the rinse pH = 4. Next, 5.0 g of pre-oxidized EG and 200 mL of 98% H_2SO_4 were suspended in an ice bath and 15 g of $KMnO_4$ was then slowly added to the mixture. Subsequently, the system was transferred to an oil bath and the mixture was heated to 40 °C under stirring for 2.5 h. The reaction was terminated with addition of 700 mL of DI water and 10 mL of 30% H_2O_2. The resulting suspension was centrifuged with 1.0 M HCl to obtain a yellow paste-like product. The product was re-dispersed in DI water, followed by centrifugation. This process was repeated until the rinse pH = 4. The resulting graphene oxide in water formed a gel-like dispersion.

2.3. Preparation of amyloid fibrils

The β-lactoglobulin (βLG) amyloid fibrils were prepared via the adapted literature procedure.[36] Typically, 2.0 wt% of βLG solution in dilute HCl (pH = 2) was heated at 90 °C under stirring for 300 min to grow amyloid fibrils. The amyloid formation was terminated by quenching the solution into an ice bath. Thioflavin T (ThT) fluorescent assay was conducted to confirm the formation of amyloid fibrils. ThT intensity of the amyloid solution was measured using JASCO FP-6500 spectrofluorometer with an excitation filter of 430 nm and 480 nm emission filter. An increased intensity in the amyloid solution was observed (SI-Fig. 1).

2.4. Preparation of GO-βLG amyloid hybrid membranes

Stock solutions of GO-βLG hybrids were prepared at room temperature from physical mixing of 0.025 wt% GO dispersion and 0.025 wt% βLG amyloid solution at pH = 2 with varying GO:βLG ratios. The stock solutions were kept at 4 °C before membrane fabrication. Typically, the mixture was filtered through a poly(ether sulfone) substrate (PES, 47 mm, 0.03 μm, Sterlitech) under pressurized conditions at 4 bar using a dead-end pressure-stirred cell (HP 4750, Sterlitech). The resultant membrane was dried in the desiccator over night before characterization and testing. In this work, the average thickness of the membrane was about 100 nm and the effective surface area of the membrane was 1.73×10^{-3} m^2.

2.5. Membrane characterization

Fourier transform infrared spectroscopy (FT-IR) spectra of GO-βLG amyloid hybrids at different amyloid fibril loadings were collected using Nicolet iS20 FT-IR spectrometer in attenuated total reflection mode (ATR) at a resolution of 4 cm^{-1} of 32 scans. X-ray diffraction (XRD) patterns were acquired in a reflection mode with 1.54 Å CuKα using Siemens D5000 diffractometer and the *d*-spacing was calculated using the Bragg equation. Atomic force microscopic (AFM) images of the membrane morphology were obtained on an Asylum Research Molecular Force Probe 3D (MFP-3D) microscope. Silicon cantilevers with force constants of 12–70 Nm^{-1} were used. The height retrace, amplitude retrace and phase retrace images were acquired and analyzed using Gwyddion Scanning Probe Microscopy (SPM) open-source software.

2.6. Nanofiltration performance

Nanofiltration performance in terms of the flux rate, rejection rate and fouling ratio was tested using a dead-end pressure stirred cell (HP 4750, Sterlitech) under nitrogen pressure. Before each test, the membrane was cleaned by fluxing Milli-Q water for 30 min. The filtration performance of the membrane was conducted by filtering 10 mL of the initial feed. The flux rate was calculated using equation [40]

$$Flux\ rate\ (J) = \frac{V}{t \times A} \quad (1)$$

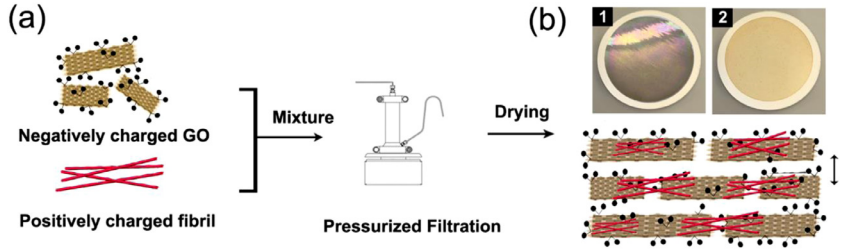

Scheme 1. (a) Schematic illustration of the fabrication of amyloid-intercalated GO membranes. The mixture of GO sheets and βLG amyloid fibrils were dispersed in nanopure water and deposited onto a PES support membrane using pressurized filtration. (b) Schematic illustration of GO-βLG hybrid membranes and photographs of GO membrane (b1) and GO-βLG hybrid membrane (b2).

V is the volume of solution filtered, t is the filtration time, and A is the effective area of the membrane. The rejection rate was calculated from the concentration difference between the pre-filtered and post-filtered solutions under 4.0 bar using equation [40]

$$Rejection\ rate\ (\%) = \left(\frac{\boldsymbol{c_0} - \boldsymbol{c_f}}{\boldsymbol{c_0}}\right) \times 100\ \% \quad (2)$$

c_o represents the initial concentration of the solution before filtration, while c_f is the concentration of the solution after filtration. For salt tests, three salts including copper(II) chloride ($CuCl_2$), cobalt(II) nitrate ($Co(NO_3)_2$) and sodium sulfate (Na_2SO_4), at a concentration of 1.0 mM were used and the electrical conductivity was measured using a conductivity meter (ECTestr 11+, Oakton) to determine the concentration. For dye tests, four organic dyes including Alcian blue (AB), methylene blue (MB), congo red (CR), and methyl orange (MO) with concentrations corresponding to absorbance of 1.0 at the wavelength of maximal absorbance was used. The chemical structure of each dye is shown in SI-Fig. 2. The absorbance maximum of each dye was measured before and after filtration using Cary-Win UV–vis spectrophotometer to determine the concentration.

To assess antifouling properties of the membrane, 20 mL of bovine serum albumin (BSA) at a concentration of 2 mg/mL was filtered through the membrane. Three periods of water flux were recorded and each period ran 40 min. First, the pure water flux (J_0) of the membrane was measured, followed by the measurement of the foulant solution flux (J_1) by filtering BSA solution through the membrane. After complete filtration, the membrane was washed sufficiently by Milli-Q water and then the pure water flux (J_2) was collected again. The antifouling performance was evaluated in terms of the flux recovery ratio (*FRR*), total fouling ratio (R_t), reversible fouling ratio (R_r) and irreversible fouling ratio (R_{ir}) using equations [20]

$$FRR = \frac{J_2}{J_0} \times 100\% \quad (3)$$

$$R_t = \frac{J_0 - J_1}{J_0} \times 100\% \quad (4)$$

$$R_r = \frac{J_2 - J_1}{J_0} \times 100\% \quad (5)$$

$$R_{ir} = \frac{J_0 - J_2}{J_0} \times 100\% \quad (6)$$

3. Results and discussion

We fabricated amyloid-intercalated GO membranes from the stable dispersions of hybrid materials composed of GO sheets and βLG amyloid fibrils onto a porous poly(ether sulfone) (PES) support membrane using pressure-assisted filtration, as shown in Scheme 1. Typically, GO nanosheets and βLG amyloid fibrils were dispersed separately in nanopure water at room temperature under pH = 2 to form stable dispersions, which were then mixed at a certain mass ratio to form dispersions of GO-βLG hybrids. When the GO: βLG ratio was lower than 3:1, the dispersions of hybrid materials gradually phase-separated showing a clear top phase of water and a dark bottom phase of hybrid precipitates (Fig. 1a). The observed sedimentation and precipitation is attributed to electrostatic interactions between negatively charged GO sheets and positively charged βLG amyloid fibrils [36]. The complexation between GO and βLG amyloid fibrils was confirmed using FTIR (SI-Fig. 3). With increasing the loading of βLG amyloid fibrils, the intensity of carbonyl vibration of GO at ~1730 cm^{-1} decreases and the intensity of amide II vibration of βLG amyloid fibrils at ~1534 cm^{-1} increases. When the GO:βLG ratio was higher than 3:1, the dispersions of hybrid materials became completely stable without significant sedimentation even after one year (Fig. 1a). We believe that the excess of GO sheets after complexing with βLG amyloid fibrils serves as a surfactant to stabilize the GO-βLG hybrid dispersion [41]. To fabricate homogeneous GO-βLG amyloid hybrid membranes, four GO:βLG ratios were selected to prepare stable hybrid dispersions with βLG amyloid fibrils: 0 wt% (1:0 GO:βLG), 5 wt% (95:5 GO:βLG), 15 wt% (85:15 GO:βLG), and 25 wt% (3:1 GO:βLG). The resulting membranes were ~100 nm in thickness. The neat GO membrane exhibited reflective metallic coloration, while the GO-βLG hybrid membrane displayed homogeneity across the surface of the membrane (Scheme 1b). Surface topographic analysis by AFM revealed that the neat GO membrane had the wrinkled surfaces while the GO-βLG hybrid membrane showed flatten surfaces containing nanoscale βLG amyloid fibrils (Fig. 1b). This observation is consistent with the literature report on amyloid induced suppression of instability of GO sheets [36]. During the membrane formation, βLG amyloid fibrils interact with GO sheets through electrostatic interactions and thereafter are intercalated in the stacked GO laminated structures to suppress wrinkling of GO sheets [20]. We quantitively investigated the surface roughness of the membrane in terms of average roughness, as shown in Fig. 1c. As the βLG fibril loading increases from 0 wt% to 25 wt%, the surface roughness of membranes decrease from 21 nm to 16 nm, indicating that the intercalated βLG amyloid fibrils effectively stabilize GO sheets [39]. The resultant GO-βLG hybrid membrane was mechanically robust and no degradation occurred after filtration. On the contrary, the neat GO membrane was instable and readily disintegrated after filtration (SI-Fig. 4).

Fig. 2a shows XRD data of the interlayer spacing of dried membranes versus βLG amyloid fibril loading. The interlayer spacing was calculated from the Bragg peak at $2\theta \sim 10^{\circ}$ (SI-Fig. 5). The neat GO membrane displays an average interlayer spacing of 8.88 Å. The incorporation of βLG amyloid fibrils into GO membranes expands the average interlayer spacing up into 9.15 Å. A consequence of enlarged interlayer spacing between GO sheets is the formation of larger 2D nanochannel networks and additional pathways for water permeation [2,5]. We examined the fil-

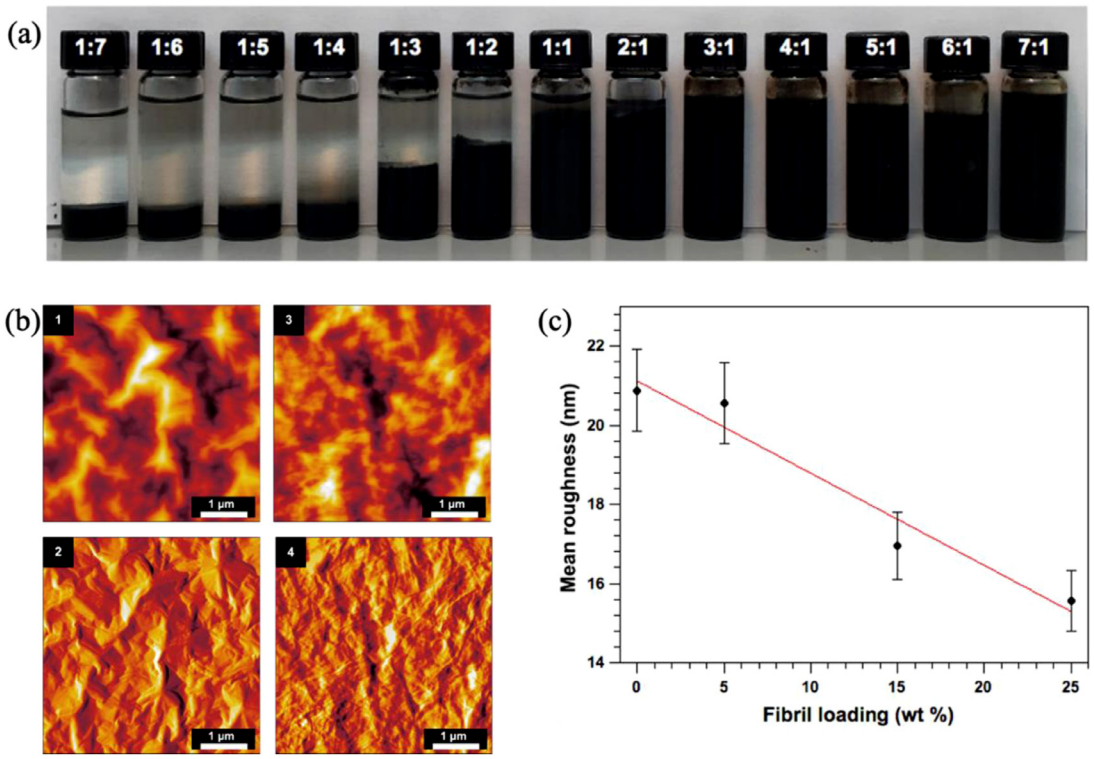

Fig. 1. (a) Photograph of dispersion of GO-βLG hybrids at pH = 2 with different GO: βLG mass ratios, ranging from 1:7 to 7:1 after one year physical mixing. (b) (b1) and (b2) are AFM images of neat GO membrane in height and amplitude modes, respectively, and (b3) and (b4) are AFM images of GO-βLG hybrid membrane containing 25wt% amyloid fibrils in height and amplitude, respectively. The amyloid fibrils are shown as the fine fibril texture in (b4). (c) Plot of surface roughness of membranes versus amyloid fibril loading. Error bars represent ranges of measured values.

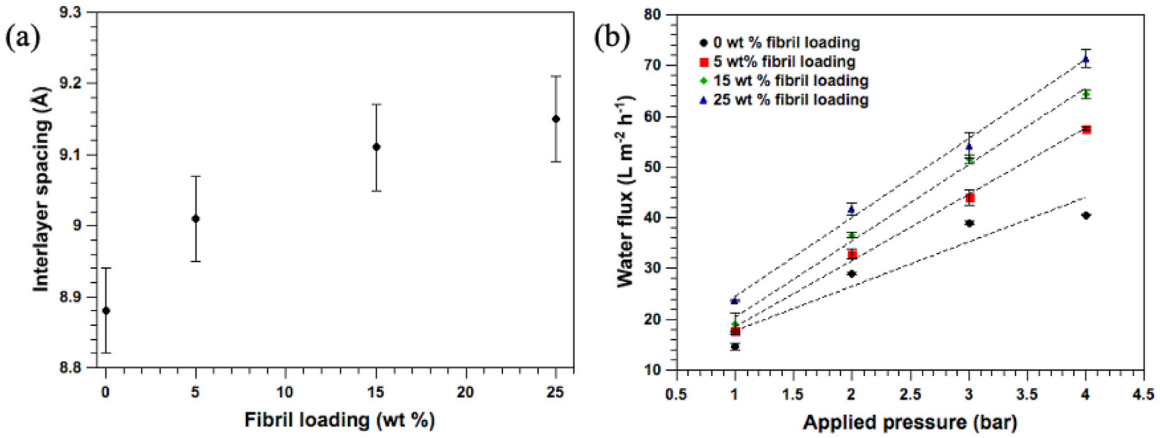

Fig. 2. (a) Interlayer spacing of membranes obtained by X-ray diffraction (XRD) versus amyloid fibril loading. (b) Water flux rate versus pressure applied in the membranes with different amyloid fibril loadings as shown in Fig. 2(b). Error bars represent ranges of standard deviations.

tration performance of hybrid membranes containing different βLG amyloid fibrils under applied pressures from 1.0 to 4.0 bar, as shown in Fig. 2b. The water flux through neat GO and amyloid intercalated GO membranes increase more or less linearly with increasing applied pressure. This observation is in good agreement with Hagen-Poiseuille model of fluid flow through multilayered laminar membranes [12]. Intercalation of amyloid fibrils into GO membranes also results in an increment of water flux. The permeance was obtained from the slope of linear fit of the data. The neat GO membrane exhibits an average water permeance of 8.8 $L \cdot m^{-2} \cdot hr^{-1} \cdot bar^{-1}$, while the GO-$\beta$LG hybrid membrane demonstrates enhanced water permeance with increasing βLG amyloid fibril loading. The average water permeance can reach 15.6 $L \cdot m^{-2} \cdot hr^{-1} \cdot bar^{-1}$ when the βLG amyloid fibril loading is 25 wt%. This observation is consistent with enlarged interlayer spacing and reduced surface wrinkling of GO sheets in hybrid membranes. Enlarged interlayer spacing between GO sheets generates more free volume for water diffusion, which results in a higher water content and a higher water flux [6]. The flattened surface of GO sheets with intercalation of βLG amyloid fibrils, furthermore, provides low-friction water transport channels. In addition, water transport through multilayered GO sheets may also be influenced by oxygen-rich functional groups [5]. The bulky carboxyl functional groups (4.0 Å) on the edges of GO sheets are highly reactive, hydrophilic, and have a high binding energy with water, resulting in steric hindrance to impede water flux [5]. In the GO-βLG hybrid membrane, a reduction in the proportion of free, negatively-charged carboxyl groups due to electrostatic interactions between

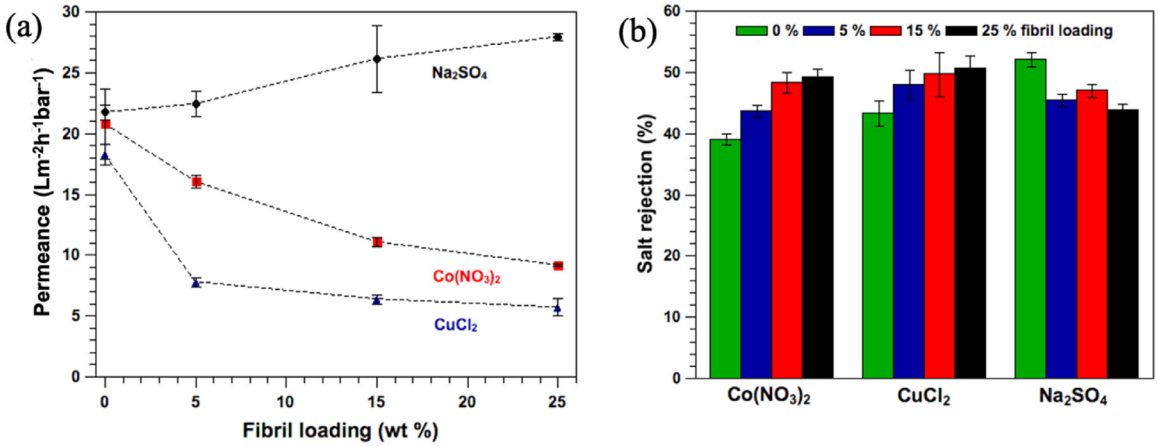

Fig. 3. (a) Salt solution permeance versus amyloid fibril loading and (b) salt rejection rate versus amyloid fibril loading for three salts: $Co(NO_3)_2$, $CuCl_2$ and Na_2SO_4. Dashed lines guide eyes only. Error bars represent ranges of measured values.

negatively charged GO sheets and positively charged βLG amyloid fibrils may reduce such steric hindrance and therefore water flux becomes faster. Thus, nanofiltration in GO-βLG hybrid membranes is improved due to the combination of an increase in interlayer spacing, a decrease in GO sheet wrinkling, and a reduction in water-binding functional groups.

It has been reported that the incorporation of amyloid fibrils into membranes is effective for removing heavy metal ions during water purification [37]. To evaluate the removal performance of heavy metal ions in amyloid-intercalated GO membranes, we selected two salts containing heavy metal ions, $Co(NO_3)_2$ and $CuCl_2$. For comparison, we also examined a well-studied salt without heavy metal ions, Na_2SO_4. Fig. 3 displays the salt filtration results of GO-βLG hybrid membranes with different amyloid fibrils. The neat GO membrane shows the salt solution permeance in the range of 18–22 $L{\cdot}m^{-2}{\cdot}hr^{-1}{\cdot}bar^{-1}$ and exhibit a moderate salt rejection in the range of 39–51%, following the order of Na_2SO_4 (51%) > $CuCl_2$ (43%) ~ $Co(NO_3)_2$ (39%). It has been well-recognized that the combination of size exclusion hindrance and Donnan electrostatic exclusion is dominant in ion transport through nanofiltration membranes [42]. Generally, when the hydrated radii of ions are larger than 4.5 Å, the interlayer spacing of neat GO membranes plays an important role in ionic sieving and rejection of the ions back into the solution. However, when the hydrated radii of ions are below 4.5 Å, the ions are readily passed through the nanochannels [5]. Since the hydrated radii of ions in this work follow the order of Cu^{2+} (4.19 Å) > SO_4^{2-} (3.8 Å) > Na^+ (3.58 Å) > NO_3^- (3.4 Å) > Co^{2+} (3.35 Å) > Cl^- (3.3 Å), the size steric exclusion alone is insufficient to remove these ions and thus the Donnan electrostatic exclusion plays determinative roles. On the basis of Donnan exclusion theory, the negatively charged GO membrane will exclude A_2B salts containing the divalent anion (B^{2-}) much more than AB_2 salts containing the divalent cation (A^{2+}) [42]. As such, the valence ratio of anion and cation (Z^-/Z^+) of salts is used to evaluate their electrostatic interactions with the charged membrane. The Z^-/Z^+ ratio of salts in this work follows the order of Na_2SO_4 (2:1) > $Co(NO_3)_2$ (1:2) ~ $CuCl_2$ (1:2). Thus, the neat GO membrane repels Na_2SO_4 stronger than $Co(NO_3)_2$ and $CuCl_2$ and thus the salt reject rate of Na_2SO_4 is greater than those $Co(NO_3)_2$ and $CuCl_2$.

In the βLG amyloid-intercalated GO membranes, the salt permeance of Na_2SO_4 increases with amyloid fibril content while $Co(NO_3)_2$ and $CuCl_2$ display decreased salt permeation, as shown in Fig. 3a. In general, the higher the permeance is, the lower the reject rate is [5]. In this work, the salt rejection of Na_2SO_4 decreases with amyloid fibrils while $Co(NO_3)_2$ and $CuCl_2$ demonstrate increased salt rejection as shown Fig. 3b. The intercalation of βLG amyloid fibrils into GO membranes enlarges the interlayer spacing of GO sheets, resulting in increased salt permeance of Na_2SO_4 [20]. In addition, the incorporation of positively charged amyloid fibrils decreases the charge density of negatively charged oxygenated functionalities on the GO sheets and therefore reduces Donnan exclusion effect, leading to decreased salt rejection of Na_2SO_4. When the heavy metal ions transport through the hybrid membranes, they are able to form complexes with protein amyloid fibrils through carboxyl, amine and thiol groups, further leading to reduced permeance and enhanced salt rejection. It has been reported that the βLG amyloid fibrils have effective binding sites at the cysteine 121 residue capable of adsorbing heavy metal ions, [37] and βLG also contains two histidine residue in its C-terminal region [43], which may coordinate to heavy metals. Coordination bond formation between the heavy metal ions and βLG amyloid fibrils favors the formation of complexes, resulting in lower permeation and higher rejection.

Fig. 4 shows dye separation performance of GO-βLG hybrid membranes with different amyloid fibrils. Four organic dyes were selected: methyl orange (MO) and Congo red (CR) are negatively charged, while methylene blue (MB) and Alcian blue (AB) are positively charged. The dye solution permeance of the neat GO membranes is 4–9 $L{\cdot}m^{-2}{\cdot}hr^{-1}{\cdot}bar^{-1}$, as shown Fig. 4a. It is found that the neat GO membrane demonstrates >97% rejection for all dyes, following the order of AB (99.9%) = MB (99.9%) > CR (98%) > MO (97%). Generally, the rejection mechanism of charged dyes in the GO based membranes relies on size exclusion, adsorption and electrostatic interactions [12]. The neat GO membrane in this work shows very high rejection (>97%) for all charged dyes with a hydrated radius above 5 $\mathring{A}$, suggesting all three rejection mechanisms act in tandem to separate organic dyes [20]. It is interesting that the positively charged dyes (AB and MB) exhibit slightly higher rejection than negatively charged dyes (CR and MO) in the negatively charged neat GO membranes, suggesting the adsorption plays a role.

In the βLG amyloid-intercalated GO membranes, the dye permeance increases with amyloid fibril content as shown Fig. 4a. The fast permeation with amyloid fibrils is attributed to enlarged interlayer spacing of amyloid intercalated membranes. The dye rejection in hybrid membranes remains >97% as in the neat GO membranes, except for negatively-charged MO that shows slightly decreased rejection with amyloid fibrils (Fig. 4b). We believe that the Donnan exclusion effect plays a role in the decreased MO rejection with

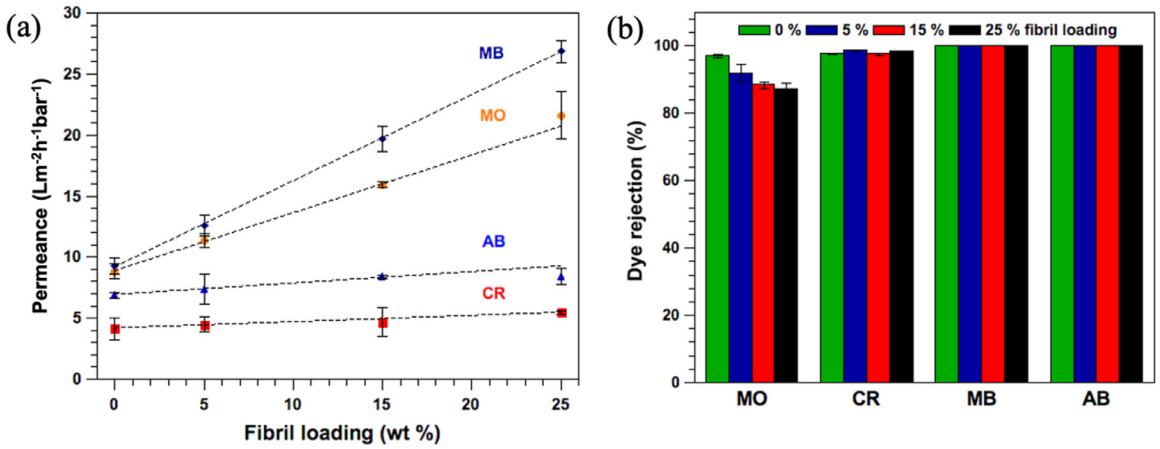

Fig. 4. (a) Dye solution permeance versus amyloid fibril loading and (b) dye rejection rate versus amyloid fibril loading for four dyes: methyl orange (MO, 327.3 g/mol) and Congo red (CR, 696.7 g/mol) are negatively charged, while methylene blue (MB, 319.85 g/mol) and Alcian blue (AB, 1298.9 g/mol) are positively charged (For interpretation of the references to color in this figure legend, the reader is referred to the web version of this article.).

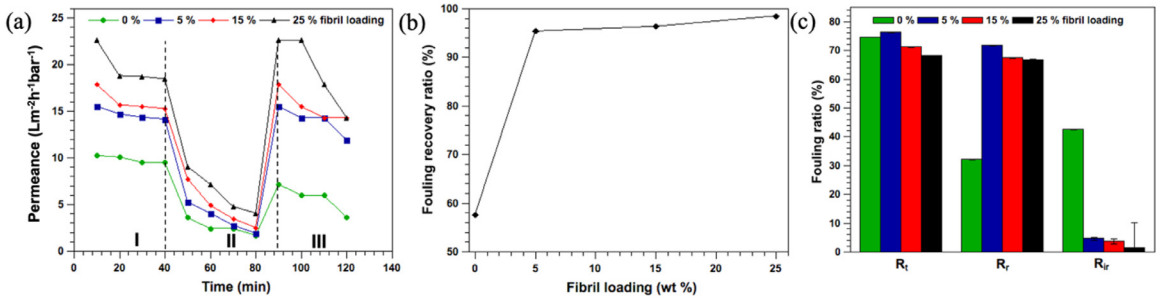

Fig. 5. Fouling resistance of amyloid intercalated GO membranes. (a) Plots of permeance versus time for three periods: pure water flux (I) before feeding the foulant solution, foulant solution flux (II) and pure water flux (III) after hydraulic washing, (b) plot of flux recovery rate (*FRR*) versus amyloid fibril loading, and (c) fouling ratio versus amyloid fibril loading for total fouling ratio (R_t), reversible fouling ratio (R_r) and irreversible fouling ratio (R_{ir}).

amyloid fibril content, because the incorporation of amyloid fibrils into GO membranes decreases the negative charge density of membranes and provide additional nanochannels for dye separation. For dyes of MB, AB and CR, the rejection changes little with amyloid fibrils, indicating that the adsorption mechanism is dominant for MB, AB and CR [20]. It has been well-known that binding of these dyes to amyloid fibrils occurs through non-covalent interactions [44–46]. It is noteworthy that the hybrid membranes are sufficiently strong to be cleaned after testing by ethanol, acetone and water. The preliminary data shows that the hybrid membranes have little physical damage and the dye rejection has little change after five consecutive cycles (SI-Fig. 6) while the maximum cycle in this work can reach 12 consecutive cycles with little disintegration under certain conditions. Further optimization of membrane fabrication is warranted.

Fouling resistance is critical to membrane applications in water treatment [47]. In this work, we used bovine serum albumin (BSA) as a model foulant to evaluate antifouling performance of the designed membrane. As shown in Fig. 5a, three periods of water permeation are recorded before feeding the foulant solution (I), during filtration of the foulant solution (II) and after filtering the foulant solution (III). In the period I, the water permeance for hybrid membranes increases with amyloid fibrils because of the enlarged interlayer spacing between GO sheets as discussed before. In the period II, the foulant solution is fed into the system and the solution permeance sharply decreases. In the period III, the foulant solution is completely filtered and the pure water permeance rises to a certain extent of recovery. To this end, the antifouling performance of the membrane is evaluated using the flux recover ratio (FRR) as shown in Fig. 5b. The neat GO membrane shows a moderate recovery of water flux and FRR is 58%. With 5% amyloid fibrils, the hybrid membrane demonstrates a significant rise in the flux recovery ratio and FRR reaches 95%, indicating remarkably enhanced fouling resistance [20]. In other words, the filtering capacity of the hybrid membrane is readily recovered by hydraulic washing. Further increasing amyloid fibrils of hybrid membranes, the flux recovery ratio tends to reach a plateau. In general, the fouling of the membrane is attributed to absorption of foulants on the membrane by strong interactions between the two [20]. In this work, the incorporation of amyloid fibrils into GO membranes can reduce interactions between BSA and GO sheets and thus increase fouling resistance. In addition, the surface roughness of the membrane decreases with amyloid fibrils (Fig. 1c), further increasing the antifouling performance as the foulants are less likely to stick to a smooth surface [20].

To further understand the membrane fouling mechanism, we have evaluated the fouling of the membrane in terms of fouling ratio including total fouling ratio (R_t), reversible fouling ratio (R_r) and irreversible fouling ratio (R_{ir}) as shown in Fig. 5c. The neat GO membrane shows $R_t \sim 75\%$, $R_r \sim 32\%$ and $R_{ir} \sim 42\%$. As the molecular size of BSA is much larger than the nanochannel size of GO membranes, the observation that the irreversible fouling (R_{ir}) is higher than reversible fouling (R_r) may be attributed to strong molecular interactions between BSA and GO such as ionic interactions and hydrogen bonding [20]. Incorporation of amyloid fibrils into GO membranes results in reduction of total fouling (R_t). In contrast to the neat GO membrane, the reversible fouling (R_r) in the hybrid membranes contributes most to the total fouling. As addressed before, the incorporation of amyloid fibrils decreases the charge density of oxygenated functionalities on the GO sheets.

As such, the foulant BSA has much weaker interactions with GO sheets in the hybrid membrane than the neat GO membrane and therefore the irreversible fouling (R_{ir}) significantly decreases. To this end, the hybrid membrane exhibits high hydraulic reversibility.

4. Conclusion

We have reported the fabrication of amyloid-intercalated graphene oxide hybrid membranes and evaluated nanofiltration performance in terms of flux rate, permeance, rejection rate and fouling ratios. The hybrid membranes are mechanically robust and smooth compared to the neat graphene oxide membrane. The incorporation of amyloid fibrils into the graphene oxide membrane enlarges the nanochannels between graphene oxide sheets and stabilize the membrane, which allows fast water transport. The hybrid membranes exhibit enhanced rejection of heavy metal ions and retain high dye rejection. In addition, the graphene oxide membranes change from irreversible fouling to reversible fouling upon intercalated with amyloid fibrils and the flux recovery of resulting hybrid membranes can reach >95%. This work opens opportunities to fabricate mechanically robust graphene oxide-based membranes with enhanced nanofiltration for water purification. We believe this work provides fundamental understanding of hybrid membranes containing both 1D and 2D nanostructures leading towards practical applications of wastewater treatment.

Acknowledgments

The work is supported by the Cal Poly Research, Scholarly, and Creative Activities (RSCA) program and the National Science Foundation (NSF) under CBET-1510207. A.C.L thanks financial support of Cal Poly William and Linda Frost Scholarship.

Supplementary materials

Supplementary material associated with this article can be found, in the online version, at doi:10.1016/j.cartre.2021.100135.

References

[1] J.R. Werber, C.O. Osuji, M. Elimelech, Materials for next-generation desalination and water purification membranes, Nat. Rev. Mater. 1 (2016), doi:10.1038/natrevmats.2016.18.
[2] Y. Wei, Y. Zhang, X. Gao, Z. Ma, X. Wang, C. Gao, Multilayered graphene oxide membrane for water treatment: a review, Carbon 139 (2018) 964–981 N. Y., doi:10.1016/j.carbon.2018.07.040.
[3] X. Li, B. Zhu, J. Zhu, Graphene oxide based materials for desalination, Carbon 146 (2019) 320–328 N. Y., doi:10.1016/j.carbon.2019.02.007.
[4] A. Anand, B. Unnikrishnan, J.Y. Mao, H.J. Lin, C.C. Huang, Graphene-based nanofiltration membranes for improving salt rejection, water flux and antifouling–a review, Desalination 429 (2018) 119–133, doi:10.1016/j.desal.2017.12.012.
[5] T. Yang, H. Lin, K.P. Loh, B. Jia, Fundamental transport mechanisms and advancements of graphene oxide membranes for molecular separation, Chem. Mater. 31 (2019) 1829–1846, doi:10.1021/acs.chemmater.8b03820.
[6] W. Li, L. Zhang, X. Zhang, M. Zhang, T. Liu, S. Chen, Atomic insight into water and ion transport in 2D interlayer nanochannels of graphene oxide membranes: implication for desalination, J. Membr. Sci. 596 (2020) 117744, doi:10.1016/j.memsci.2019.117744.
[7] D.W. Kim, J. Jang, I. Kim, Y.T. Nam, Y. Jung, H.T. Jung, Revealing the role of oxygen debris and functional groups on the water flux and molecular separation of graphene oxide membrane: a combined experimental and theoretical study, J. Phys. Chem. C 122 (2018) 17507–17517, doi:10.1021/acs.jpcc.8b03318.
[8] A. Gogoi, T.J. Konch, K. Raidongia, K. Anki Reddy, Water and salt dynamics in multilayer graphene oxide (GO) membrane: role of lateral sheet dimensions, J. Membr. Sci. 563 (2018) 785–793, doi:10.1016/j.memsci.2018.06.031.
[9] C. Sun, M. Liu, B. Bai, Molecular simulations on graphene-based membranes, Carbon 153 (2019) 481–494 N. Y., doi:10.1016/j.carbon.2019.07.052.
[10] M. Hu, B. Mi, Enabling graphene oxide nanosheets as water separation membranes, Environ. Sci. Technol. 47 (2013) 3715–3723, doi:10.1021/es400571g.
[11] J. Wang, P. Zhang, B. Liang, Y. Liu, T. Xu, L. Wang, B. Cao, K. Pan, Graphene oxide as an effective barrier on a porous nanofibrous membrane for water treatment, ACS Appl. Mater. Interfaces. 8 (2016) 6211–6218, doi:10.1021/acsami.5b12723.
[12] A. Akbari, P. Sheath, S.T. Martin, D.B. Shinde, M. Shaibani, P.C. Banerjee, R. Tkacz, D. Bhattacharyya, M. Majumder, Large-area graphene-based nanofiltration membranes by shear alignment of discotic nematic liquid crystals of graphene oxide, Nat. Commun. 7 (2016) 1–12, doi:10.1038/ncomms10891.
[13] Y.H. Xi, J.Q. Hu, Z. Liu, R. Xie, X.J. Ju, W. Wang, L.Y. Chu, Graphene oxide membranes with strong stability in aqueous solutions and controllable lamellar spacing, ACS Appl. Mater. Interfaces 8 (2016) 15557–15566, doi:10.1021/acsami.6b00928.
[14] K.S. Abraham, J. Vasu, C.D. Williams, K. Gopinadhan, Y. Su, C.T. Cherian, J. Dix, E. Prestat, S.J. Haigh, I.V. Grigorieva, P. Carbone, A.K. Geim, R.R. Nair, Tunable sieving of ions using graphene oxide membranes, Nat. Nanotechnol. 12 (2017) 546–550.
[15] H. Huang, Z. Song, N. Wei, L. Shi, Y. Mao, Y. Ying, L. Sun, Z. Xu, X. Peng, Ultrafast viscous water flow through nanostrand-channelled graphene oxide membranes, Nat. Commun. 4 (2013), doi:10.1038/ncomms3979.
[16] A. Morelos-Gomez, R. Cruz-Silva, H. Muramatsu, J. Ortiz-Medina, T. Araki, T. Fukuyo, S. Tejima, K. Takeuchi, T. Hayashi, M. Terrones, M. Endo, Effective NaCl and dye rejection of hybrid graphene oxide/graphene layered membranes, Nat. Nanotechnol. 12 (2017) 1083–1088, doi:10.1038/nnano.2017.160.
[17] P. Sun, R. Ma, W. Ma, J. Wu, K. Wang, T. Sasaki, H. Zhu, Highly selective charge-guided ion transport through a hybrid membrane consisting of anionic graphene oxide and cationic hydroxide nanosheet superlattice units, NPG Asia Mater. 8 (2016) 1–10, doi:10.1038/am.2016.38.
[18] X. Chen, M. Qiu, H. Ding, K. Fu, Y. Fan, Reduced graphene oxide nanofiltration membrane intercalated by well-dispersed carbon nanotubes for drinking water purification received, Nanoscale 8 (2016) 5696–5705, doi:10.1039/x0xx00.
[19] Y. Yang, X. Yang, L. Liang, Y. Gao, H. Cheng, X. Li, M. Zou, A. Cao, R. Ma, Q. Yuan, X. Duan, Large-area graphene-nanomesh/ders of magnitude thinner than the commercial membrane would undergo substantially larger stress (19). Therefore, the applications of ultrathin carbon-nanotube hybrid membranes 2D membranes for practical water treatment remai, Science 364 (80) (2019) 1057–1062.
[20] Y. Han, Y. Jiang, C. Gao, High-flux graphene oxide nanofiltration membrane intercalated by carbon nanotubes, ACS Appl. Mater. Interfaces 7 (2015) 8147–8155, doi:10.1021/acsami.5b00986.
[21] M. Sivakumar, D.K. Liu, Y.H. Chiao, W.S. Hung, Synergistic effect of one-dimensional silk nanofiber and two-dimensional graphene oxide composite membrane for enhanced water purification, J. Membr. Sci. 606 (2020) 118142, doi:10.1016/j.memsci.2020.118142.
[22] Y. Lyu, Q. Zhang, Z. Wang, J. Pu, A graphene oxide nanofiltration membrane intercalated with cellulose nano-crystals, Bioresources 13 (2018) 9116–9131, doi:10.15376/biores.13.4.9116-9131.
[23] L.R. Volpatti, M. Vendruscolo, C.M. Dobson, T.P.J. Knowles, A clear view of polymorphism, twist, and chirality in amyloid fibril formation, ACS Nano 7 (2013) 10443–10448, doi:10.1021/nn406121w.
[24] J. King, C. Haase-Pettingell, D. Gossard, Protein folding and misfolding, Am. Sci. 90 (2002) 445–453, doi:10.1511/2002.5.445.
[25] T.P.J. Knowles, R. Mezzenga, Amyloid fibrils as building blocks for natural and artificial functional materials, Adv. Mater. (2016) 6546–6561, doi:10.1002/adma.201505961.
[26] C. Wang, M. Zhang, X. Mao, Y. Yu, C.X. Wang, Y.L. Yang, Nanomaterials for reducing amyloid cytotoxicity, Adv. Mater. 25 (2013) 3780–3801, doi:10.1002/adma.201301210.
[27] C. Li, R. Mezzenga, The interplay between carbon nanomaterials and amyloid fibrils in bio-nanotechnology, Nanoscale 5 (2013) 6207–6218, doi:10.1039/c3nr01644g.
[28] B. Choi, S.W. Lee, K. Eom, Nanomechanical behaviors and properties of amyloid fibrils, 1 (2016) 53–64.
[29] B. Choi, G. Yoon, S.W. Lee, K. Eom, Mechanical deformation mechanisms and properties of amyloid fibrils, Phys. Chem. Chem. Phys. 17 (2015) 1379–1389, doi:10.1039/c4cp03804e.
[30] T.J. Paul, Z. Hoffmann, C. Wang, M. Shanmugasundaram, J. DeJoannis, A. Shekhtman, I.K. Lednev, V.K. Yadavalli, R. Prabhakar, Structural and mechanical properties of amyloid beta fibrils: a combined experimental and theoretical approach, J. Phys. Chem. Lett. 7 (2016) 2758–2764, doi:10.1021/acs.jpclett.6b01066.
[31] L.R. Volpatti, T.P.J. Knowles, Polymer physics inspired approaches for the study of the mechanical properties of amyloid fibrils, J. Polym. Sci. Part B Polym. Phys. 52 (2014) 281–292, doi:10.1002/polb.23428.
[32] X. Wu, M. Li, Z. Li, L. Lv, Y. Zhang, C. Li, Amyloid-graphene oxide as immobilization platform of Au nanocatalysts and enzymes for improved glucose-sensing activity, J. Colloid Interface Sci. 490 (2017) 336–342, doi:10.1016/j.jcis.2016.11.058.
[33] R.A. Taheri, Y. Akhtari, T. Tohidi Moghadam, B. Ranjbar, Assembly of gold nanorods on HSA amyloid fibrils to develop a conductive nanoscaffold for potential biomedical and biosensing applications, Sci. Rep. 8 (2018) 1–10, doi:10.1038/s41598-018-26393-6.
[34] D. Ghosh, P. Dutta, C. Chakraborty, P.K. Singh, A. Anoop, N.N. Jha, R.S. Jacob, M. Mondal, S. Mankar, S. Das, S. Malik, S.K. Maji, Complexation of amyloid fibrils with charged conjugated polymers, Langmuir 30 (2014) 3775–3786, doi:10.1021/la404739f.
[35] S. Bolisetty, M. Arcari, J. Adamcik, R. Mezzenga, Hybrid amyloid membranes for continuous flow catalysis, Langmuir 31 (2015) 13867–13873, doi:10.1021/acs.langmuir.5b03205.

[36] C. Li, J. Adamcik, R. Mezzenga, Biodegradable nanocomposites of amyloid fibrils and graphene with shape-memory and enzyme-sensing properties, Nat. Nanotechnol. 7 (2012) 421–427, doi:10.1038/nnano.2012.62.
[37] S. Bolisetty, R. Mezzenga, Amyloid-carbon hybrid membranes for universal water purification, Nat. Nanotechnol. 11 (2016) 365–371, doi:10.1038/nnano.2015.310.
[38] W.S. Hummers, R.E. Offeman, Preparation of Graphitic Oxide, J. Am. Chem. Soc. 80 (1958) 1339, doi:10.1021/ja01539a017.
[39] Y. Luo, G.A. Braggin, G.T. Olson, A.R. Stevenson, W.L. Ruan, S. Zhang, Nematic order drives macroscopic patterns of graphene oxide in drying drops, Langmuir 30 (2014) 14631–14637, doi:10.1021/la503670e.
[40] M. Sivakumar, D.K. Liu, Y.H. Chiao, W.S. Hung, Synergistic effect of one-dimensional silk nanofiber and two-dimensional graphene oxide composite membrane for enhanced water purification, J. Membr. Sci. 606 (2020) 118142, doi:10.1016/j.memsci.2020.118142.
[41] L.J. Cote, J. Kim, V.C. Tung, J. Luo, F. Kim, J. Huang, Graphene oxide as surfactant sheets, Pure Appl. Chem. 83 (2011) 95–110, doi:10.1351/PAC-CON-10-10-25.
[42] M. Zhang, K. Guan, Y. Ji, G. Liu, W. Jin, N. Xu, Controllable ion transport by surface-charged graphene oxide membrane, Nat. Commun. 10 (2019) 1–8, doi:10.1038/s41467-019-09286-8.
[43] B.Y. Qin, M.C. Bewley, L.K. Creamer, H.M. Baker, E.N. Baker, G.B. Jameson, Structural basis of the tanford transition of bovine β-lactoglobulin, Biochemistry 37 (1998) 14014–14023, doi:10.1021/bi981016t.
[44] A. Pomerance, G. Slavin, J. McWatt, Experience with the sodium sulphate alcian blue stain for amyloid in cardiac pathology, J. Clin. Pathol. 29 (1976) 22–26, doi:10.1136/jcp.29.1.22.
[45] S.C. How, Y.H. Cheng, C.H. Lo, J.T. Lai, T.H. Lin, Z. Bednarikova, A. Antosova, Z. Gazova, J.W. Wu, S.S.S. Wang, Exploring the effects of methylene blue on amyloid fibrillogenesis of lysozyme, Int. J. Biol. Macromol. 119 (2018) 1059–1067, doi:10.1016/j.ijbiomac.2018.08.038.
[46] E.I. Yakupova, L.G. Bobyleva, I.M. Vikhlyantsev, A.G. Bobylev, Congo Red and amyloids: history and relationship, Biosci. Rep. (2019) 39, doi:10.1042/BSR20181415.
[47] L.F. Fang, N. Kato, H.Y. Yang, L. Cheng, S. Hasegawa, S. Jeon, H. Matsuyama, Evaluating the antifouling properties of poly(ether sulfone)/sulfonated poly(ether sulfone) blend membranes in a full-size membrane module, Ind. Eng. Chem. Res. 57 (2018) 4430–4441, doi:10.1021/acs.iecr.8b00114.